Vacuum 227 (2024) 113375

Contents lists available at ScienceDirect

Vacuum

journal homepage: www.elsevier.com/locate/vacuum

Resistive switching properties of a nanostructured layer of mixed ZrO_2 phases obtained in low-pressure arc discharge plasma

I.V. Karpov [a,b], L. Yu Fedorov [a,b,*], A.K. Abkaryan [a], S.M. Zharkov [a,c], M.S. Molokeev [a,c], A.A. Ivanenko [c], I.V. Nemtsev [b,c], L.A. Irtyugo [a]

[a] Siberian Federal University, 660041, Krasnoyarsk, Russian Federation
[b] Federal Research Center Krasnoyarsk Scientific Center of the Siberian Branch of the Russian Academy of Sciences, 660036, Krasnoyarsk, Russian Federation
[c] Kirensky Institute of Physics, Federal Research Center KSC SB RAS, 660036, Krasnoyarsk, Russian Federation

ARTICLE INFO

Handling Editor: Prof. L.G. Hultman

Keywords:
Zirconium oxide
Vacuum arc
Physical vapor deposition
Phase stability

ABSTRACT

The controlled vacuum-arc synthesis of zirconium dioxide (ZrO_2) nanoparticles is considered, which makes it possible to regulate the percentage ratio of the monoclinic and tetragonal phases. The samples were characterized using XRD analysis, SEM, HRTEM analysis, FT-IR analysis, TG/DTA analysis and EPR spectroscopy. It has been established that the formation of the tetragonal phase is associated with the formation of a large number of oxygen vacancies formed due to high-speed quenching of nanoparticles. Reducing the operating gas pressure in a vacuum chamber from 180 Pa to 30 Pa makes it possible to obtain nanoparticles up to 2 nm in size. The synthesized ZrO_2 nanoparticles do not contain foreign impurities and when heated, the weight loss is up to 7 %. The process of local resistive switching in the contact of an atomic force microscope (AFM) probe to a nanostructured $ZrO_{(2-x)}$ layer on a conducting substrate has been studied. Cyclic current-voltage characteristics demonstrate the existence of stable states of high and low resistance, switched by changing the polarity of the applied voltage. The coexistence of the *m*- and *t*-ZrO_2 phases (and the resulting oxygen nonstoichiometry in the interboundary regions) provides conditions for the formation/destruction of a filament from oxygen vacancies, which determine the conductivity of the dielectric in the LRS state.

1. Introduction

According to modern concepts, the physics of the phenomenon of resistive switching in metal-insulator-metal structures with a dielectric layer of Zr, Hf, Ta oxides significantly depends on the presence of a large number of oxygen vacancies in their structure [1–4]. It is with them that the ability of dielectrics to conduct current is associated with the ordered alignment of chains of vacancies (filaments) between the electrodes of the memristor cell. In this case, the formation of a conducting state is, firstly, stable, i.e. persists for a long time when the voltage is removed, and, secondly, it is reversible - by applying a voltage of reverse polarity (in the case of bipolar resistive switching), the conducting filament is destroyed, and the cell goes into a state of high resistance, which is also stable for a long time. Such a reversible restructuring of the structure resistance can potentially be implemented in efficient non-volatile resistive random access memory (ReRAM) devices, as well as neurocomputer systems.

According to Refs. [5,6], the formation and stability of the tetragonal phase is explained by the presence of oxygen ion vacancies inside ZrO_2 nanoparticles. Thus, by increasing the proportion of the tetragonal phase in ZrO_2 nanoparticles, the process of formation of oxygen vacancies can be controlled.

In this article, we study the effect of operating pressure in a vacuum chamber on the phase composition of ZrO_2 nanoparticles and their resistive switching properties. Many works are devoted to the synthesis and study of the stability of the phase composition of ZrO_2 [7–9]. The most important conclusion is that the stability of the observed phases largely depends on the synthesis methods used to produce the materials and on the sizes of the resulting particles [10].

Thus, research in the field of control of ZrO_2 phases and their relationship with resistive switching properties becomes relevant. In this work, we present a method for the synthesis of metastable tetragonal phase ZrO_2. We found that the tetragonal ZrO_2 phase can be formed without the addition of a stabilizing impurity. Depending on the pressure in the plasma-chemical reactor, nanoparticles with a tetragonal ZrO_2 phase are formed.

* Corresponding author. Siberian Federal University, 660041, Krasnoyarsk, Russian Federation.
E-mail address: sfu-unesco@mail.ru (L.Y. Fedorov).

https://doi.org/10.1016/j.vacuum.2024.113375
Received 17 April 2024; Received in revised form 21 May 2024; Accepted 6 June 2024
Available online 6 June 2024

2. Experimental section

2.1. Preparation of samples

The oxidation of Zr to form ZrO_2 is a highly exothermic reaction. The enthalpy of formation of ZrO_2 is −1100.6 kJ/mol, so synthesis in a low-pressure arc discharge plasma is very effective [11–14]. To synthesize ZrO_2 nanoparticles, a vacuum chamber with a plasma-arc evaporator mounted on the side wall was used, connected to an inverter power source that provides an arc discharge current of 100 A (Fig. 1). The experimental setup and the dependence of the properties of the powder on the spraying conditions are discussed in detail in Refs. [15–17]. The cathode, 80 mm in diameter and 100 mm in length, consisted of a zirconium alloy with a purity of 99.99 % and was installed on a water-cooled copper current lead. The reaction chamber dimensions are 0.6 m in diameter and 0.6 m in height, with double walls and stainless steel flanges.

The samples were obtained at a pressure in a vacuum chamber of 180, 130, 80 and 30 Pa (hereinafter designated sample N1, N2, N3, N4) with argon as a plasma-forming gas. Argon/oxygen gas flow rates were 3000/600, 2000/400, 1200/240, 300/60 ml/min, which provided the specified pressure levels for the corresponding samples. Oxygen was supplied to the reactor in such a way as to form a uniform shell around the plasma torch. The reactor was pre-evacuated to a base pressure of 10^{-3} Pa. The reaction products were collected for 20 min on a water-cooled hemispherical stainless steel collector located at a distance of 120 mm from the cathode. The substrate temperature during arc discharge operation is 393 K.

2.2. Characterization methods

The powder diffraction data of all samples (N1, N2, N3, N4) for Rietveld analysis were collected at room temperature with a Bruker D8 Advance with Cu-Kα radiation (λ = 0.1540 nm) and linear detector. The step size of 2θ was 0.01°, and the counting time was 0.2 s per step. To analyze the crystal structure of experimental X-ray diffraction patterns, PDF-4+ databases from the International Center for Diffraction Data (ICDD) were used.

The size and shape of the synthesized particles were assessed by scanning electron microscopy using Hitachi S-5500 equipment and a Hitachi TM4000Plus desktop electron microscope with an energy-dispersive (EDS) microanalysis system.

Transmission electron microscopy (TEM) of ZrO_2 nanoparticles was carried out on a JEOL JEM-2100 high-resolution electron microscope operating at an accelerating voltage of 200 kV.

IR spectral studies were carried out on a Vertex 80 V vacuum Fourier spectrometer (Bruker) in the range 5000–370 sm^{-1}, with a spectral resolution of 0.2 sm^{-1}. Sample preparation was carried out as follows.

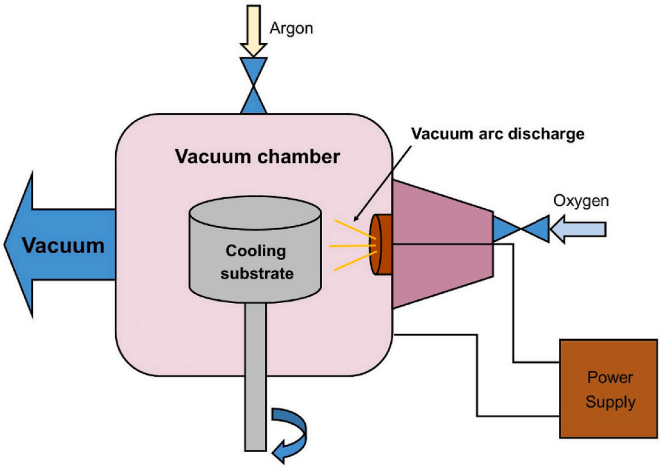

Fig. 1. Scheme of the synthesis process of experimental samples.

1. Thoroughly grind KBr crystals in an agate mortar and agate pestle.
2. Thoroughly grind 0.008–0.02 g of the measured sample in an agate mortar and agate pestle.
3. Mixing and additional grinding of the prepared KBr powder and sample in an agate mortar and agate pestle. The range of proportions is 1/10-1/200 by mass depending on the optical density in the measured IR range.
4. Final drying of the resulting powder for up to 30 min in a microwave oven at minimum heating mode (10 %).
5. Compress approximately 0.2 g of the mixture into a 13 mm mold, resulting in a transparent or translucent tablet with a diameter of 13 mm.

Thermal analysis was carried out on samples obtained at a gas mixture pressure of 30, 80, 130 Pa. The measurements were carried out on a complex for DSC/TG analysis from NETZSCH, using corundum crucibles with lids. Measuring range 30–1200°C, heating rate in air 20 K/min. Additionally, to eliminate the oxidation process, the sample obtained at a gas mixture pressure of 30 Pa was heated at the same temperature conditions in an argon environment.

Electron paramagnetic resonance (EPR) spectra were measured at room temperature on a Bruker ELEXSYS 580 instrument with a resonant frequency of 9.27 GHz (wave number 0.31 cm^{-1}) in the magnetic field induction range from 480 to 6000 G.

Studies of resistive switching were carried out on a scanning probe microscope SMM-2000 (Proton, Russia). Scanning was carried out in contact atomic force microscopy (CAFM) mode with conductive cantilevers (0.01–0.025 Ohm•cm Antimony (n) doped Si with Pt/Ir coating and nominal tip radius 10 nm).

The samples had a layered structure. The substrate was standard p-Si (001) plates coated with a layer of silicon dioxide SiO_2 (thickness ~500 nm) and a platinum conducting layer Pt (50 nm) acting as the bottom electrode. The resistive layer is a polycrystalline film of zirconium dioxide (ZrO_2), deposited using the technology of sample N4. The thickness of the ZrO_2 layer was ~30 nm and was controlled by the time the substrates were exposed to the plasma cloud. The microscope cantilever acted as the top electrode when measuring local current-voltage characteristics. The contact area is estimated to be ~100 nm^2. Scanning field 4 × 4 μm. To avoid the influence of anodic oxidation upon injection of electrons from a cantilever [18], which can reduce the current through the dielectric, all electrical measurements in this work were carried out in a closed volume with dry nitrogen purging at atmospheric pressure and room temperature.

The experiment was carried out as follows. A topographic image of the sample was obtained, and then cyclic current-voltage characteristics were taken at arbitrary points on the surface. First, at a selected point, the cantilever was brought into contact with the sample and a voltage of up to $U_t = +15$ V was applied to it to carry out electroforming. In this case, the current It flowing through the AFM probe was limited to a given value of 15 nA (related to the saturation current of the AFM amplifier). After holding for 10 s, U_t was reset to zero. Electroforming moves the device from a high-resistance HRS state to a low-resistance (LRS) or ON state with resistive switching enabled.

Next, the presence of resistive switching was investigated by measuring a series of cyclic current-voltage characteristics (I–V characteristics) $I_t(U_t)$ with a linear sweep U_t from $U_{min} = -6$ V < U_{RESET} to $U_{max} = +6$ V > U_{SET} and back to U_{min}, etc. Here, U_{SET} and U_{RESET} are the threshold voltage values for switching from a high resistance state to a low resistance state and back from LRS to HRS, respectively. Due to sample heterogeneity (defect concentration, variable thickness, etc.), U_{SET} and U_{RESET} may differ at different points in the sample. Therefore, when changing the point of measurement of the current-voltage characteristic, the values of U_{min} and U_{max} were adjusted to achieve stable

resistive switching.

In each of the states (LRS and HRS), a series of current It values were measured during several rewriting cycles – I_{ON} and I_{OFF}, respectively. These values were measured after applying switching voltages for 3–5 s to the contact of the AFM probe with the sample. 10–20 values of I_{ON} and I_{OFF} were recorded, which were then averaged.

3. Results and discussion

3.1. Characterization analysis

3.1.1. XRD analysis

Almost all peaks, besides small amount of tiny unknown impurity peaks, were indexed by monoclinic and tetragonal phase of ZrO_2 and Zr_3O. Therefore, these structures were taken as starting model for Rietveld refinement which was performed using TOPAS 4.2 [19]. The atom coordinates were fixed during refinement because structures are known. Refinements were stable and gave low *R*-factors (Table 1, Fig. 2).

Rietveld refinement was utilized to accurately determine the crystal size for all samples. The instrumental peak broadening was assessed using a Si standard, and subsequently factored into the crystal size estimation process in TOPAS 4.2.

In samples N1, N2, N3, and N4, the monoclinic ZrO_2 phase exhibits average crystal sizes of 30.9(7) nm, 19.0(6) nm, 16.8(6) nm, and 13.1(2) nm, respectively. On the other hand, the ZrO_2 tetragonal phase in the same samples has average crystal sizes of 8.7(1) nm, 8.2(2) nm, 6.8(2) nm, and 5.4(1) nm, respectively. The numbers in brackets represent the estimated standard deviation (ESD).

Table 1
Main parameters of processing and refinement of the samples.

Sample	Phase	Weight, %	Space Group	Cell parameters (Å), Cell Volume (Å^3)	R_{wp}, R_p, χ^2
N1	ZrO_2	89(1)	$P2_1/c$	a = 5.157 (8), b = 5.203 (8), c = 5.324 (8), β = 99.113 (9) V = 141.0 (4)	6.35, 4.94, 1.25
	ZrO_2	11(1)	$P4_2/nmc$	a = 3.603 (7), c = 5.166 (15), V = 67.1 (3)	
N2	ZrO_2	76(1)	$P2_1/c$	a = 5.176 (3), b = 5.215 (3), c = 5.327 (3), β = 98.90 (1) V = 142.1 (2)	6.60, 5.26, 1.26
	ZrO_2	24(1)	$P4_2/nmc$	a = 3.616 (3), c = 5.173 (4), V = 67.6 (1)	
N3	ZrO_2	45(1)	$P2_1/c$	a = 5.156 (4), b = 5.207 (4), c = 5.325 (4), β = 99.178 (9) V = 141.1 (2)	6.23, 4.90, 1.37
	ZrO_2	52(1)	$P4_2/nmc$	a = 3.599 (3), c = 5.197 (4), V = 67.3 (1)	
	Zr_3O	3(1)	$P6_322$	a = 5.629 (4), c = 5.216 (4), V = 143.1 (2)	
N4	ZrO_2	42(1)	$P2_1/c$	a = 5.153 (5), b = 5.198 (5), c = 5.325 (5), β = 99.08 (2) V = 140.8 (2)	6.32, 5.00, 1.26
	ZrO_2	53(1)	$P4_2/nmc$	a = 3.597 (3), c = 5.193 (4), V = 67.2 (1)	
	Zr_3O	5(1)	$P6_322$	a = 5.633 (5), c = 5.5211 (4), V = 143.2 (3)	

As XRD analysis showed, the formation of crystalline phases depends on the operating pressure in the vacuum chamber and on the O_2 concentration. With a decrease in the operating pressure in the vacuum chamber (and, accordingly, the O_2 concentration), the proportion of the tetragonal phase increases from 11 to 53 %. According to Refs. [5,6], the formation and stability of the tetragonal phase is explained by the presence of oxygen ion vacancies inside ZrO_2 nanoparticles.

In Fig. 2 you can see that at high pressure in the vacuum chamber (Sample N1), the monoclinic phase predominates. While a decrease in pressure promotes the growth of the tetragonal phase (Sample N4). The change in the crystalline phase, based on the change in operating pressure in the reactor, can be associated with the cluster chemistry of vapor phase condensation [20]. Zirconium ions mix in the plasma column with excited oxygen atoms and enter into a chemical reaction, forming Zr–O molecules, which then quickly cool and become crystallization centers [15]. Since the formation or elimination of oxygen ion vacancies at low or high oxygen pressure is time-limited, the kinetics of the chemical reactions involved (oxygen diffusion) plays an important role in the number of monoclinic-tetragonal or tetragonal-monoclinic phase transformations.

Another important factor in the formation of the ZrO_2 phase composition is the cooling rate of the synthesized nanoparticles, which directly depends on the thermal conductivity of the gas mixture.

3.1.2. SEM, HRTEM analysis

The morphology of the synthesized samples is presented in Figs. 3 and 4. The experimental results obtained clearly indicate a qualitative difference in the powders obtained at different pressures of the gas mixture in a vacuum chamber.

Fig. 3 shows a microphotograph of ZrO_2 (sample N1) obtained at a gas mixture pressure of 180 Pa. The synthesized nanoparticles have a very large size range from 30 nm to 1 μm. The appearance of large particles is most likely due to the fact that in order to obtain powders at a pressure of 180 Pa to maintain a stable combustion of the arc discharge, it is necessary to increase the voltage across the discharge gap, which led to the transition from a diffuse plasma column to a classic “arched” column. At the same time, associations of cathode spots and their groups began to appear. As a result, upon evaporation from the surface of the zirconium cathode, a plasma state is formed containing one-, two-, and three-fold charged particles. In addition to charged particles, the plasma may contain a droplet component, fragments of the cathode material. The multicomponent nature of the plasma creates conditions for the formation of a nonequilibrium condensate in composition and structure. On the contrary, the morphology of sample N4 is a homogeneous condensate, without inclusions of the microdroplet fraction. This indicates the effectiveness of dispersing the material coming from the cathode in the plasma.

Fig. 4 shows high-resolution transmission microscopy images, particle distribution diagrams and size distribution density functions of ZrO_2 nanoparticles obtained at different gas mixture pressures (130, 80 and 30 Pa). As follows from the results obtained, ZrO_2 nanopowder is highly agglomerated spherical particles. Particle sizes vary from 2 to 32 nm. The largest particles are formed at a gas mixture pressure of 130 Pa. Over the entire pressure range, particles are characterized by a mixed normal and lognormal particle size distribution. This indicates two competing mechanisms of condensation of particles from the vapor-plasma phase: cluster and vapor [21]. A mixed distribution density function is presented, which is the sum of the lognormal and normal distribution density functions with adjustable parameters [15].

The particle size distribution function is directly related to the mechanisms of nanoparticle synthesis [22]. Depending on the method of nanoparticle synthesis, the distribution function can differ significantly. In this regard, three processes of nanoparticle formation can be distinguished: non-diffusion, diffusion and coagulation [23,24]. The

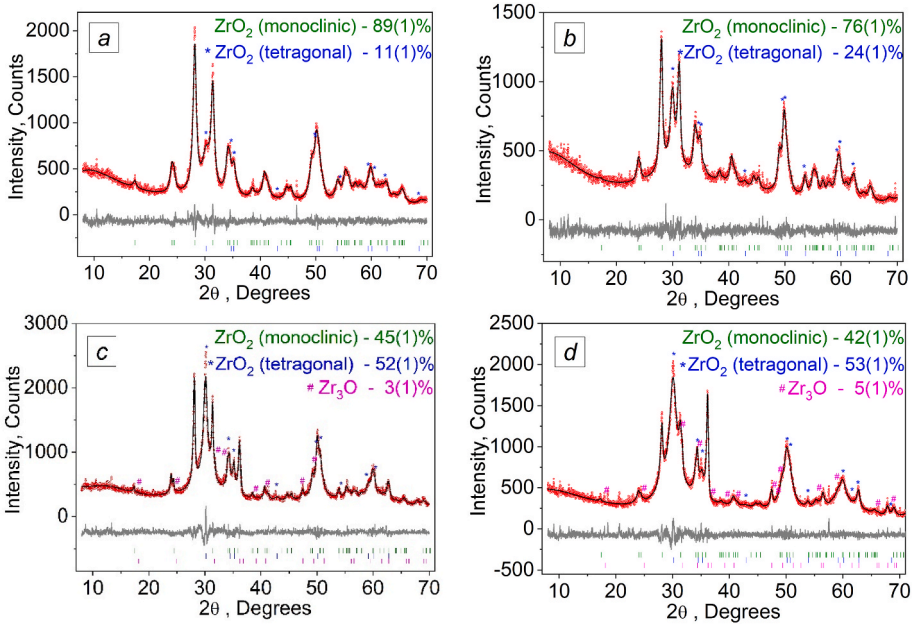

Fig. 2. Difference Rietveld plot of sample: *a*) N1 (180 Pa); *b*) N2 (130 Pa); *c*) N3 (80 Pa); *d*) N4 (30 Pa).

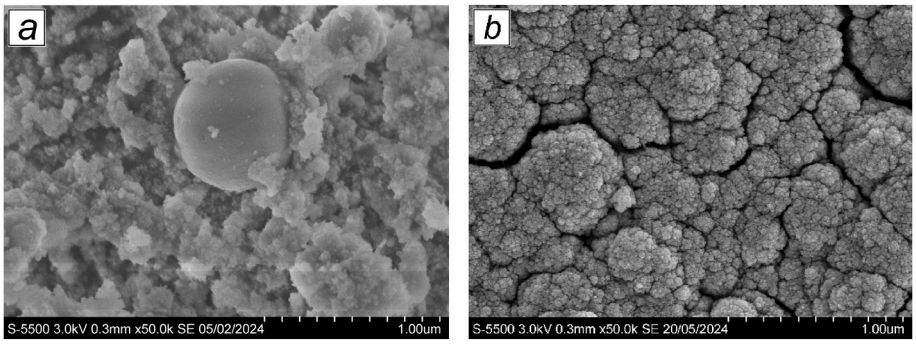

Fig. 3. SEM image of a ZrO_2 samples: obtained at a gas mixture pressure of 180 Pa (Sample N1 – *a*), and 30 Pa (Sample N4 – *b*).

occurrence of the first process is associated with the phase boundary and the reaction rate, depending on adsorption, reevaporation, etc. In this case, the size of nanoparticles depends on the residence time in the synthesis area.

If the second mechanism predominates, the growth of nanoparticles is possible through mass transfer of atoms over long distances. In this case, the size of nanoparticles changes proportionally to the rate of diffusion of atoms. And in the case of convection, the size of nanoparticles can be proportional to the convection speed. The sizes of nanoparticles depend on the residence time in the synthesis zone.

The third mechanism is determined mainly by the collision of clusters and nanoparticles of various sizes, followed by adhesion, rapid recrystallization, and coalescence. This process is usually modeled as the merging of liquid droplets using a viscous flow mechanism (liquid-like coalescence). The rate of synthesis of nanoparticles using this mechanism is very high and is aimed at reducing the surface energy. It is assumed that the melting temperature of nanoparticles is significantly lower than large particles and a liquid-like or amorphous film is always present on the surface.

For practical applications, a combination of normal and lognormal distributions can be used, since during condensation from the plasma-vapor phase, clusters first grow by the first two mechanisms due to the layer-by-layer growth of atoms, and then by cluster coagulation. As a rule, if the average particle size is less than 10 nm, then such nanopowders are characterized by a normal distribution. For larger particles, there is an increasing deviation of the experimental data from the normal distribution towards the log-normal distribution. For large particles of the order of 30 nm, the coagulation mechanism of nanoparticle growth is predominant. Thus, we can conclude that for nanoparticles of plasma-chemical synthesis, the most probable is a mixed particle size distribution.

3.1.3. FT-IR analysis

Using IR spectroscopy, the results of which are presented in Fig. 5, the features of the chemical structure of molecular bonds of nano-sized zirconium dioxide powders obtained at different pressures in a vacuum chamber (30, 80, 130 Pa) were studied. All samples exhibit an absorption band near 3408 sm^{-1}, 1626 sm^{-1} and 1384 sm^{-1}, which is related to the stretching vibrations of bound –OH groups. The presence of such groups is indirect evidence of the high surface activity of the obtained zirconium dioxide nanoparticles, which manifests itself in them at large specific surface areas. In this case, a large number of free bonds are formed on the surface of the particles and exposed atoms, such as Zr and O in nanoparticles, could most likely adsorb OH^- and H^+ ions from their environment, resulting in the formation of a surface enriched with active OH^- in groups. Weak absorption in the region of 2955 sm^{-1}, 2923 sm^{-1}, 2854 sm^{-1} and 1466 sm^{-1} is due to the presence of C–H stretching vibrations in the samples. These compounds are most likely formed due to the injection of a small amount of vacuum oil into the reaction chamber from a high-vacuum diffusion pump.

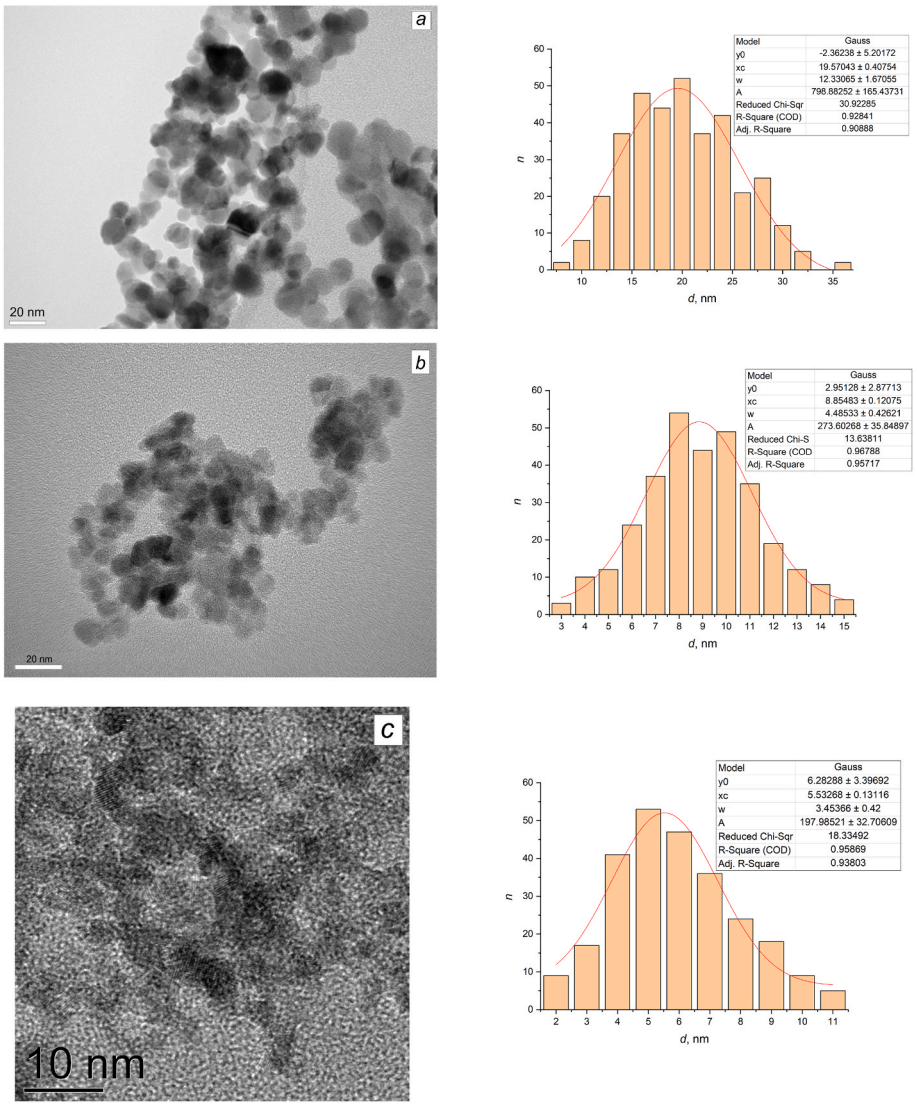

Fig. 4. TEM image of ZrO_2 nanoparticles synthesized at different pressures of the gas mixture: *a* – Sample N2 (130 Pa), *b* – Sample N3 (80 Pa), *c* – Sample N4 (30 Pa) and the corresponding histograms of particle size distribution.

Absorption frequencies for metal oxides are, as a rule, in the region below 1000 sm^{-1}. The spectra contain absorption bands characteristic of ZrO_2, in the region of 739 sm^{-1} and 588 sm^{-1}, caused by interatomic stretching vibrations of the crystalline core. It is also known [25] that the position of the absorption band caused by vibrations of *Me*–O bonds in the IR absorption spectra depends on the concentration of excess *Me* in the *Me*–O compound. In our case, stretching vibrations of the Zr–O bond are observed in nanoparticles obtained at pressures in the reaction vacuum chamber at 30 and 80 Pa, at a frequency of 1048 sm^{-1}, which indicates a lack of oxygen in ZrO_2 nanoparticles.

Thus, we can conclude that sample N4 of ZrO_2 nanoparticles does not contain foreign impurities, and only absorbed moisture is present on the surface. In addition to the main phase and moisture, samples N3 and N2 contain a small amount of alkanes.

Regarding the presence of traces of vacuum oil in some samples, the following can be said. Vacuum oil leaking into a vacuum chamber is a rare occurrence. Most likely, it is associated with the operating features of the diffusion pump. The synthesis of nanopowders occurs in fore-vacuum mode. Under such conditions, the oil vapor jets have a high density. Their interaction with the pumped air at high pressure occurs in the boundary layer and is turbulent in nature. As a result, vacuum oil may enter the deposited samples. Also, a likely cause of oil leakage may be its overheating. In this case, destruction and partial decomposition of macromolecules occurs. Such fractions are more volatile and have a higher vapor pressure.

3.1.4. Simultaneous thermogravimetric and differential thermal (TG/DTA) analysis

Fig. 6 shows thermograms of ZrO_2 nanopowder obtained at different pressures of the gas mixture. The sample obtained at 180 Pa was not considered to be of scientific interest.

In sample N3, a sharp loss of mass (12 %) is observed. Most likely, this is due to the simultaneous evaporation of moisture and hydrocarbons contained in small quantities in the sample, in accordance with IR spectroscopy. In this case, a hydration reaction may occur. Above a temperature of 100 °C and up to 1200 °C, the mass of the sample increases by 10.9 %. This is due to the oxidation of Zr_3O suboxide with a broad exothermic peak at a maximum of 470 °C, as well as the crystallization of the amorphous phase of zirconium dioxide. At a temperature of 930 °C, the beginning of an endothermic peak associated with the $m \rightarrow t$ transition of the ZrO_2 phase is observed. The transition is completed at a temperature of 1150 °C.

For sample N4, the endothermic effect, associated with the evaporation of water, begins almost at room temperature and has a peak at

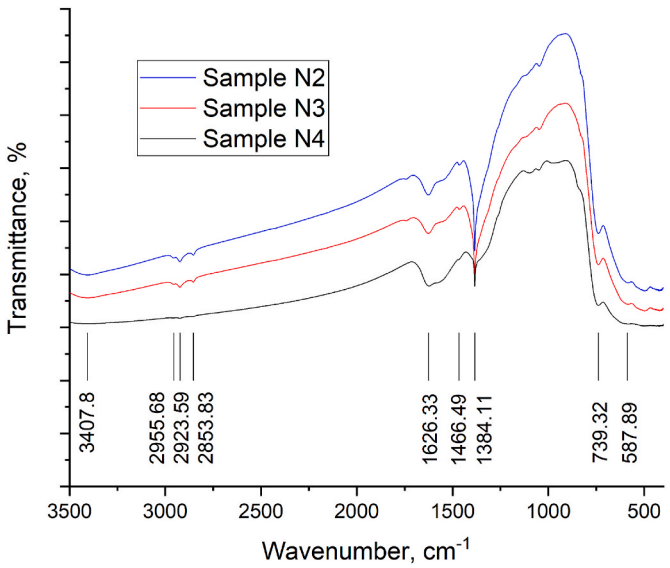

Fig. 5. Fourier transform infrared spectroscopy (FTIR) spectra of ZrO_2 nanoparticle obtained by different gas mixture pressure.

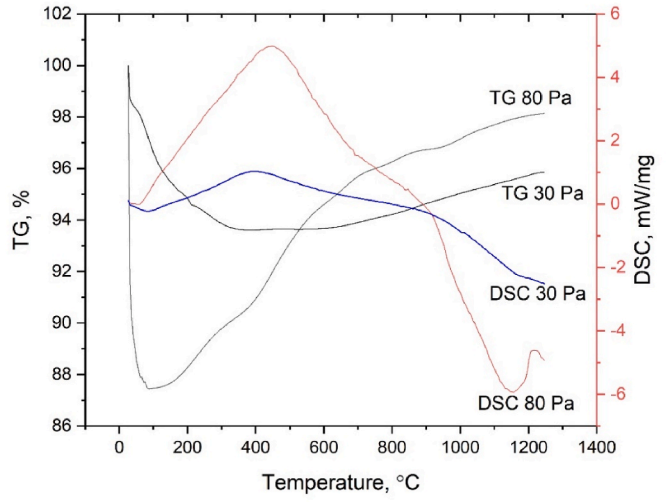

Fig. 6. TG and DSC curves of samples of ZrO_2 nanopowder obtained at different pressures of the gas mixture.

100 °C. In this case, the weight loss of the sample was 2 %. Against the background of further mass loss associated with the removal of water from the sample, a dominant exothermic effect with a maximum at 405 °C is superimposed. Most likely, as in the case of sample N3, crystallization of the amorphous phase and oxidation of Zr_3O suboxide occurs, with a subsequent increase in the mass of the sample. At a temperature of 930 °C, the beginning of an endothermic peak associated with the $m \rightarrow t$ transition is observed. The transition is completed at a temperature of 1160 °C.

In order to exclude the influence of oxidation, the N4 sample was heated in an argon environment. As in the case of heating in air, an endothermic effect is observed with a maximum of about 100 °C. The mass loss associated with water evaporation continues up to 200 °C and amounts to 7 %. With a further increase in temperature, the mass of the sample does not change. A broad exothermic effect with a maximum around 400 °C is associated with crystallization of the amorphous phase. At a temperature of 950 °C, the beginning of an endothermic peak associated with the $m \rightarrow t$ transition is observed.

Upon cooling, in all samples examined, a slight exothermic effect of a tetragonal-monoclinic phase transition with a maximum at 895 °C is observed.

Thus, TG/DTA analysis showed the thermal stability of the synthesized samples with minimal weight loss.

3.1.5. Electron paramagnetic resonance (EPR) spectroscopy

To confirm the presence of an increased concentration of oxygen vacancies in the ZrO_2 sample synthesized at a pressure of 30 Pa, the EPR method was used. The measurement results are presented in Fig. 7. In the presented spectra for samples N2 and N4, a signal with a g-factor of 1.964 is observed, characteristic of paramagnetic $4d1$ Zr^{3+} ions [26,27]. The formation of defects is most likely associated with nonequilibrium processes and high-speed quenching of nanoparticles in the plasma of a low-pressure arc discharge, as well as non-stoichiometry with respect to oxygen. In addition, the spectrum of sample N4 shows a signal with a g-factor of 2.004, corresponding to F^+ centers, i.e. electrons stabilized in oxygen vacancies of ZrO_2 [28]. Thus, the results obtained confirm the presence of an increased concentration of oxygen vacancies in sample N4. Subsequently, it will be used to study the effect of resistive switching.

3.2. Research on the effect of resistive switching

The AFM method is an effective tool for determining resistive switching characteristics in a dielectric with high lateral resolution. However, there are a number of features that must be taken into account when conducting the experiment and interpreting the results [29]. This includes limiting the voltage (15 V) that can be applied to the cantilever and which may not be enough to complete the electroforming process, especially for thick dielectric layers. Another limitation is the current measured by the microscope – within 15 nA. Obtaining statistical data may be difficult due to wear on the cantilever needle.

Fig. 8 shows a typical cyclic current-voltage characteristic of the contact of the AFM probe to the surface of the ZrO_2 film, where pronounced hysteresis is observed, characteristic of memristors with bipolar resistive switching for sample N4. In them, switching of the SET and RESET states occurs at voltages of opposite polarity. At the same time, sample N2 exhibits monotonic behavior characteristic of metal-insulator-metal structures, without resistive switching.

The U_{SET} voltage depends on the electrode material, the thickness of the resistive switching film, and the number of oxygen vacancies in it that participate in the formation of the conducting filament. The voltage

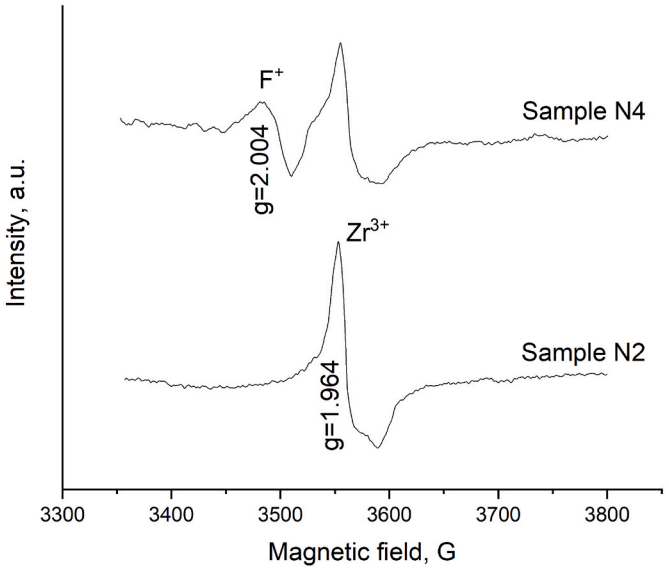

Fig. 7. EPR spectra of ZrO_2 samples.

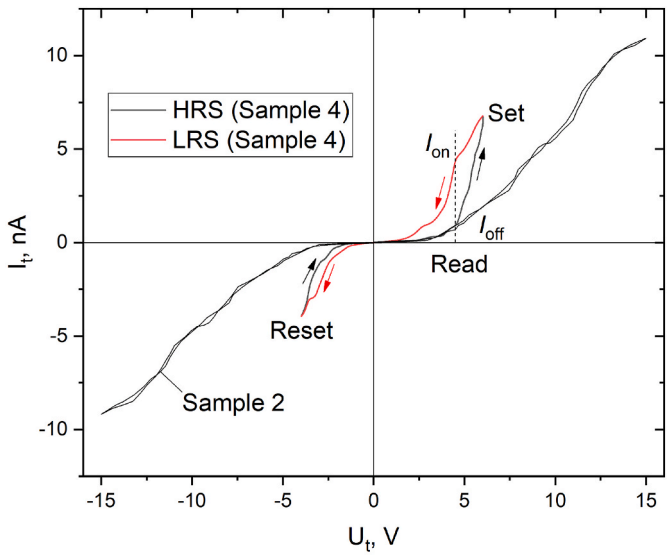

Fig. 8. Cyclic current-voltage characteristic of the contact of the AFM probe and the surface of the dielectric layer of ZrO_2 samples N2 and N4.

at which the device state was read was determined to be $U_{READ} = 4.5$ V. At this value, the window between the LRS and HRS states was largest, and, in addition, it did not lead to a device state switch (Fig. 9). The readout voltage in CAFM experiments is typically higher than for dual-electrode devices due to the much smaller contact area. When the voltage sweep did not reach the U_{SET}/U_{RESET} values and returned to zero, the device retained its state for a long time, i.e. was non-volatile.

The currently most developed model describing the effect of resistive switching in dielectric films is the thread-like model based on oxygen vacancies (Fig. 9) [30]. They participate in charge transport and are controlled by an external electric field, which determines the most preferred direction of growth of a chain of vacancies. A conductive filament is formed (SET mode – Fig. 10, *c*) when oxygen vacancies diffuse from the anode (electrode to which a voltage has been applied) to the cathode (grounded electrode) or breaks (RESET mode – Fig. 10, *d*) when oxygen vacancies migrate back. Moreover, as was shown in Ref. [31], when the filament is formed, the conductivity mechanism of the device cannot be attributed to one specific type; it is a superposition

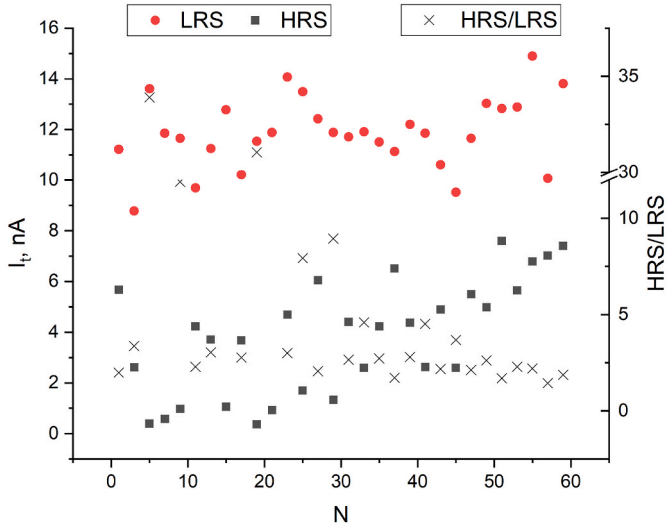

Fig. 9. Dependences of I_{ON} (●), I_{OFF} (■) and HRS/LRS ratio (×) of the contact of the AFM probe and the surface of the dielectric layer of ZrO_2 sample N4 on the number of switching cycles N during cyclic switching.

of the contributions of Poole-Frenkel conductivity, space charge limited conductivity, Schottky emission, trap tunneling and hopping conductivity. The method of obtaining the dielectric layer, temperature, applied electric field and polarity determine its contribution to the total conductivity.

Additional confirmation of this can also be found in Ref. [32]. It shows that the most energetically favorable case for the formation of a polyvacancy of oxygen (filament) is the case when a subsequent oxygen vacancy is formed near already existing vacancies. The electron released during the formation of an oxygen vacancy is localized between the two Zr atoms closest to each other and has the character of a bonding orbital. In this case, charge transport occurs through a channel of Zr ions separating vacancies in the chain, providing conductivity in the ZrO_2 dielectric.

The high electroforming voltage (up to +15 V in our experiment) that must be applied to the freshly prepared film is associated with the primary initiation of filament formation and formation. The nascent filament is localized in the region of grain boundaries - the place of the highest concentration of electric field lines, where conditions are provided for better mobility of vacancies [33]. Then it grows, connects opposite electrodes and begins to increase in diameter, transferring the cell to the LRS state. When a voltage of opposite polarity is applied, the thread breaks. However, complete dissipation of the thread throughout the entire thickness of the film does not occur. That is why the repeated transition of the dielectric to the on state is observed at a noticeably lower voltage (+6 V). Such reversible switching is usually stable for a large number of "rewrite" cycles (10^3-10^4) if the measurement is carried out in a device with two electrodes. When studying the effect of resistive switching in AFM, the number of "rewrite" cycles usually does not exceed 100 due to the degradation of the memristor properties, during which the window between the currents in the HRS and LRS states decreases, and ultimately does not allow reliably reading the cell state. In our experiment, a noticeable decrease in the difference between I_{ON} and I_{OFF} occurred after 30 cycles (Fig. 9). During cyclic studies using the AFM method, difficulties with probe positioning and wear are also observed.

The small window between the currents in the two states can be caused by the diameter of the forming filament in the case when the AFM tip is the electrode. The conductivity of such a filament is highly susceptible to any external fluctuations. With each resistive switching cycle, impurities from the electrode material penetrate into the ZrO_2 dielectric layer, leading to an increase in the I_{OFF} current in the HRS state [34]. As the number of cycles increases, the density of impurities increases so much that the conductive filament can no longer be re-oxidized. The cyclic stability of the filament is also affected by the conductive coating of the microscope cantilever. It can contaminate the dielectric layer with impurity ions due to the high current density in the probe-sample contact, also leading to cell degradation. In memristor devices with large contact areas, the current behavior and cyclic stability are less stochastic.

When the polarity changes, the filament formed by oxygen vacancies is partially destroyed. This occurs as a result of the diffusion of oxygen vacancies initiated by a change in the polarity of the external voltage. In this case, destruction occurs in the area of contact of the cantilever with the sample, where the diameter of the filament, which has a conical shape, is smaller.

4. Conclusion

A method has been developed that makes it possible to control the phase composition of both ZrO_2 nanoparticles and the resistive layer based on them. The possibility of using synthesized nanomaterials as an active element of resistive switching devices has been demonstrated. Phase heterogeneity in the ZrO_2 layer deposited using sample N4 technology contributed to the stable formation of a conductive filament. This can be caused by both the high content of oxygen vacancies in the

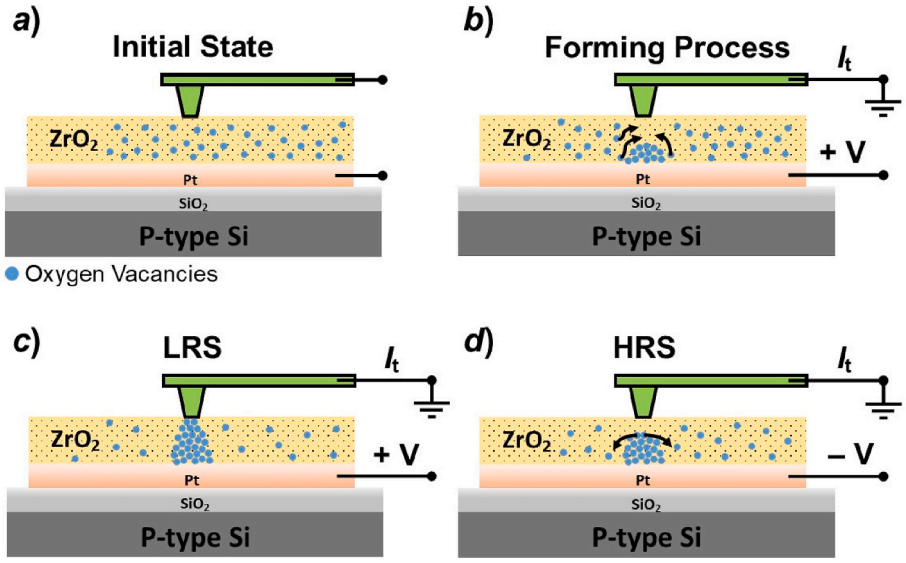

Fig. 10. Schematics of the mechanisms of resistive switching. Layer thicknesses are not shown to scale.

dielectric layer due to the coexistence of the *m*- and *t*-crystalline phases of ZrO_2 and the Zr_3O phase, and their high mobility under the action of an electric field in the grain boundaries.

CRediT authorship contribution statement

I.V. Karpov: Writing – original draft, Conceptualization. **L. Yu Fedorov:** Writing – original draft, Conceptualization. **A.K. Abkaryan:** Data curation. **S.M. Zharkov:** Data curation. **M.S. Molokeev:** Formal analysis. **A.A. Ivanenko:** Investigation. **I.V. Nemtsev:** Data curation. **L. A. Irtyugo:** Investigation.

Declaration of competing interest

The authors declare that they have no known competing financial interests or personal relationships that could have appeared to influence the work reported in this paper.

Data availability

No data was used for the research described in the article.

Acknowledgments

The work was performed with a support of the grant of the Russian Science Foundation (Project No. 24-29-00374, https://rscf.ru/project/24-29-00374/). The TEM investigations were conducted in the laboratory of electron microscopy of the SFU Joint Scientific Center.

References

[1] D. Kumar, R. Aluguri, U. Chand, T.Y. Tseng, Metal oxide resistive switching memory: materials, properties and switching mechanisms, Ceram. Int. 43 (Suppl. 1) (2017) S547–S556, https://doi.org/10.1016/j.ceramint.2017.05.289.
[2] D. Ielmini, Resistive switching memories based on metal oxides: mechanisms, reliability and scaling, Semicond. Sci. Technol. 31 (2016) 063002, https://doi.org/10.1088/0268-1242/31/6/063002.
[3] Y. Li, M. Zhang, S. Long, J. Teng, Q. Liu, H. Lv, E. Miranda, J. Suñé, M. Liu, Investigation on the conductive filament growth dynamics in resistive switching memory via a universal Monte Carlo simulator, Sci. Rep. 7 (2017) 11204, https://doi.org/10.1038/s41598-017-11165-5.
[4] A. Sawa, Resistive switching in transition metal oxides//Materials Today 11 (6) (2008) 28–36, https://doi.org/10.1016/S1369-7021(08)70119-6.
[5] S. Shukla, S. Seal, Mechanisms of room temperature metastable tetragonal phase stabilisation in zirconia, Int. Mater. Rev. 50 (1) (2005) 45–64, https://doi.org/10.1179/174328005X14267.
[6] P. Kountouros, G. Petzow, in: S.P.S. Bidwal, et al. (Eds.), Science and Technology of Zirconia V', Technomic Publishing, USA, 1993, p. 30.
[7] H.-J. Huang, M.-C. Wang, The phase formation and stability of tetragonal ZrO_2 prepared in a silica bath, Ceram. Int. 39 (2) (2013) 1729–1739, https://doi.org/10.1016/j.ceramint.2012.08.019.
[8] D.-J. Kim, T.-Y. Tien, Phase stability and physical properties of cubic and tetragonal ZrO_2 in the system ZrO_2–Y_2O_3–Ta_2O_5, J. Am. Ceram. Soc. 74 (Is. 12) (1991) 3061–3065, https://doi.org/10.1111/j.1151-2916.1991.tb04302.x.
[9] F. Lu, J. Zhang, M. Huang, F. Namavar, R.C. Ewing, J. Lian, Phase transformation of nanosized ZrO_2 upon thermal annealing and intense radiation, J. Phys. Chem. C 115 (15) (2011) 7193–7201, https://doi.org/10.1021/jp109558s.
[10] B.L. Kirsch, S.H. Tolbert, Stabilization of isolated hydrous amorphous and tetragonal zirconia nanoparticles through the formation of a passivating alumina shell, Adv. Funct. Mater. 13 (2003) 281–288.
[11] A.V. Ushakov, I.V. Karpov, A.A. Shaihadinov, L.Yu Fedorov, E.A. Goncharova, V. G. Demin, Ionization features in cathode spot region of vacuum arc, Vacuum 179 (2020) 109509, https://doi.org/10.1016/j.vacuum.2020.109509.
[12] M.A. Lieberman, A.J. Lichtenberg, Principles of Plasma Discharges and Materials Processing, John Wiley & Sons, New York, 2005, p. 757.
[13] A. Anders, Cathodic Arcs, vol. 3, Springer-Verlag New York, 2008, p. 1, https://doi.org/10.1007/978-0-387-79108-1.
[14] H.C. Miller, Vacuum arcs, IEEE Trans. Plasma Sci. 51 (Is. 7) (2023) 1585–1594, https://doi.org/10.1109/TPS.2023.3261779.
[15] A.V. Uschakov, I.V. Karpov, A.A. Lepeshev, M.I. Petrov, Plasma-chemical synthesis of copper oxide nanoparticles in a low-pressure arc discharge, Vacuum 133 (2016) 25–30, https://doi.org/10.1016/j.vacuum.2016.08.007.
[16] A.V. Ushakov, I.V. Karpov, A.A. Lepeshev, S.M. Zharkov, The influence of oxygen concentration on the formation of CuO and Cu_2O crystalline phases during the synthesis in the plasma of low pressure arc discharge, Vacuum 128 (2016) 123–127, https://doi.org/10.1016/j.vacuum.2016.03.025.
[17] I.V. Karpov, A.V. Ushakov, A.A. Lepeshev, L.Yu Fedorov, Plasma-chemical reactor based on a low-pressure pulsed arc discharge for synthesis of nanopowders, Tech. Phys. 62 (2017) 168–173, https://doi.org/10.1134/S106378421701011X.
[18] X. Blasco, D. Hill, M. Porti, M. Nafria, X. Aymerich, Topographic characterization of AFM-grown SiO_2 on Si, Nanotechnology 12 (2001) 110–112, https://doi.org/10.1088/0957-4484/12/2/307.
[19] Bruker AXS TOPAS V4, General Profile and Structure Analysis Software for Powder Diffraction Data, User's Manual. Bruker AXS, Karlsruhe, Germany, 2008.
[20] R.J. Kee, M.E. Coltrin, P. Glarborg, Chemically Reacting Flow: Theory and Practice, Wiley-Interscience, New York, 2003, p. 928.
[21] G.A. Mesyats, N.M. Zubarev, The Rayleigh–Plateau instability and jet formation during the extrusion of liquid metal from craters in a vacuum arc cathode spot, J. Appl. Phys. 117 (2015) 043302, https://doi.org/10.1063/1.4906559.
[22] W. Yang, Q. Sun, Q. Zhou, Particle modeling of vacuum arc discharges, J. Appl. Phys. 128 (2020) 060905, https://doi.org/10.1063/5.0014485.
[23] A. Simchi, R. Ahmadi, S.M. Seyed Reihani, A. Mahdavi, Kinetics and mechanisms of nanoparticle formation and growth in vapor phase condensation process// Materials &amp, Design 28 (3) (2007) 850–856, https://doi.org/10.1016/j.matdes.2005.10.017.
[24] T.K. Nguyen Thanh, N. Maclean, S. Mahiddine, Mechanisms of nucleation and growth of nanoparticles in solution, Chem. Rev. 114 (15) (2014) 7610–7630, https://doi.org/10.1021/cr400544s.
[25] G. Lucovsky, P.D. Richard, D.V. Tsu, S.Y. Lin, R.J. Markunas, Deposition of silicon dioxide and silicon nitride by remote plasma enhanced chemical vapor deposition, J. Vac. Sci. Technol. A 4 (1986) 681–688, https://doi.org/10.1116/1.573832.

[26] N.O. Korsunska, M. Baran, A. Zhuk, Yu Polishchuk, T. Stara, V. Kladko, Yu Bacherikov, Ye Venger, T. Konstantinova, L. Khomenkova, Role of paramagnetic defects in light emission processes in Y-doped ZrO_2 nanopowders, Mater. Res. Express 1 (2014) 045011, https://doi.org/10.1088/2053-1591/1/4/045011.

[27] J. Matta, J.-F. Lamonier, E. Abi-Aad, E. Zhilinskaya, A. Aboukaïs, Transformation of tetragonal zirconia phase to monoclinic phase in the presence of Fe^{3+} ions as probes: an EPR study//Physical, Chemistry Chemical Physics 1 (1999) 4975–4980, https://doi.org/10.1039/a904828f.

[28] S. Wright, R.C. Barklie, EPR characterization of defects in monoclinic powders of ZrO_2 and HfO_2, Mater. Sci. Semicond. Process. 9 (6) (2006) 892–896, https://doi.org/10.1016/j.mssp.2006.10.006.

[29] M. Lanza, A review on resistive switching in high-k dielectrics: a nanoscale point of view using conductive atomic force microscope, Materials 7 (3) (2014) 2155–2182, https://doi.org/10.3390/ma7032155.

[30] M.J. Rozenberg, M.J. Sánchez, R. Weht, C. Acha, F. Gomez-Marlasca, P. Levy, Mechanism for bipolar resistive switching in transition-metal oxides, Phys. Rev. B 81 (2010) 115101, https://doi.org/10.1103/PhysRevB.81.115101.

[31] E.W. Lim, R. Ismail, Conduction mechanism of valence change resistive switching memory, Surveyor/Electronics 4 (3) (2015) 586–613, https://doi.org/10.3390/electronics4030586.

[32] T.V. Perevalov, Simulation of the atomic and electronic structure of oxygen vacancies and polyvacancies in ZrO_2//phys, Solid State 60 (2018) 423–427, https://doi.org/10.1134/S106378341803023X.

[33] G. Bersuker, J. Yum, L. Vandelli, A. Padovani, L. Larcher, V. Iglesias, M. Porti, M. Nafría, K. McKenna, A. Shluger, P. Kirsch, R. Jammy, Grain boundary-driven leakage path formation in HfO_2 dielectrics, Solid State Electron. 65–66 (2011) 146–150, https://doi.org/10.1016/j.sse.2011.06.031.

[34] H. Lv, X. Xu, H. Liu, R. Liu, Q. Liu, W. Banerjee, H. Sun, S. Long, L. Li, M. Liu, Evolution of conductive filament and its impact on reliability issues in oxide-electrolyte based resistive random access memory, Sci. Rep. 5 (2015) 7764, https://doi.org/10.1038/srep07764.